ADVANCED MATERIALS
www.advmat.de

# Ultraflexible Wireless Imager Integrated with Organic Circuits for Broadband Infrared Thermal Analysis

*Rei Kawabata, Kou Li, Teppei Araki,* Mihoko Akiyama, Kaho Sugimachi, Nozomi Matsuoka, Norika Takahashi, Daiki Sakai, Yuto Matsuzaki, Ryo Koshimizu, Minami Yamamoto, Leo Takai, Ryoga Odawara, Takaaki Abe, Shintaro Izumi, Naoko Kurihira, Takafumi Uemura, Yukio Kawano,* and Tsuyoshi Sekitani**

**Flexible imagers are currently under intensive development as versatile optical sensor arrays, designed to capture images of surfaces and internals, irrespective of their shape. A significant challenge in developing flexible imagers is extending their detection capabilities to encompass a broad spectrum of infrared light, particularly terahertz (THz) light at room temperature. This advancement is crucial for thermal and biochemical applications. In this study, a flexible infrared imager is designed using uncooled carbon nanotube (CNT) sensors and organic circuits. The CNT sensors, fabricated on ultrathin 2.4 µm substrates, demonstrate enhanced sensitivity across a wide infrared range, spanning from near-infrared to THz wavelengths. Moreover, they retain their characteristics under bending and crumpling. The design incorporates light-shielded organic transistors and circuits, functioning reliably under light irradiation, and amplifies THz detection signals by a factor of 10. The integration of both CNT sensors and shielded organic transistors into an 8 × 8 active-sensor matrix within the imager enables sequential infrared imaging and nondestructive assessment for heat sources and in-liquid chemicals through wireless communication systems. The proposed imager, offering unique functionality, shows promise for applications in biochemical analysis and soft robotics.**

## 1. Introduction

Optical sensors play a crucial role in converting light into electrical signals, facilitating visualization and analysis. Conventional optical sensors rely on inorganic semiconductors and ferroelectric materials placed on rigid substrates, inherently lacking flexibility.[1–3] This limitation has sparked interest in the development of mechanically flexible optical sensors.[4–6] Materials such as Si and perovskites have emerged as candidates for flexible photodetectors when integrated into thin films.[7,8] The inherent flexibility of organic semiconductors, enabling them to generate photocarriers across a wide spectrum from ultraviolet (UV) to near-infrared (NIR) wavelengths, has made organic photodiodes and phototransistors particularly appealing.[1,6,9] Among the applications of flexible optical sensors, large-area imagers stand out prominently.[10–13] These imagers feature arrays capable of

R. Kawabata, T. Araki, M. Akiyama, K. Sugimachi, N. Matsuoka, T. Abe, S. Izumi, N. Kurihira, T. Uemura, T. Sekitani
SANKEN (The Institute of Scientific and Industrial Research)
Osaka University
8-1, Mihogaoka, Ibaraki-shi, Osaka 567-0047, Japan
E-mail: araki@sanken.osaka-u.ac.jp; sekitani@sanken.osaka-u.ac.jp

R. Kawabata, T. Araki, M. Akiyama, T. Sekitani
Graduate School of Engineering
Osaka University
2-1 Yamadaoka, Suita, Osaka 565–0871, Japan

The ORCID identification number(s) for the author(s) of this article can be found under https://doi.org/10.1002/adma.202309864



**DOI: 10.1002/adma.202309864**

K. Li, N. Takahashi, D. Sakai, Y. Matsuzaki, R. Koshimizu, M. Yamamoto, L. Takai, R. Odawara, Y. Kawano
Department of Electrical, Electronic, and Communication Engineering,
Faculty of Science and Engineering
Chuo University
1-13-27 Kasuga, Bunkyo-ku, Tokyo 112–8551, Japan
E-mail: kawano@elect.chuo-u.ac.jp

T. Araki, T. Uemura, T. Sekitani
Advanced Photonics and Biosensing Open Innovation Laboratory
National Institute of Advanced Industrial Science and Technology (AIST)
2-1 Yamada-Oka, Suita, Osaka 565-0871, Japan

K. Sugimachi, N. Matsuoka, T. Sekitani
Division of Applied Science, School of Engineering
Osaka University
2-1 Yamadaoka, Suita, Osaka 565–0871, Japan

S. Izumi
Graduate School of Science
Technology and Innovation
Kobe University
1-1 Rokkodai-cho, Nada-ku, Kobe, Hyogo 657–8501, Japan

adapting to objects with various shapes, enabling extensive, high-speed imaging suitable for applications ranging from internal inspections to noninvasive medical assessments.[14,15] However, many of these imagers face challenges in detecting long-wavelength infrared light, constrained by the inherent band structures of semiconductor-based photodetectors.[16–18]

Infrared light, including terahertz (THz) light, finds applications across diverse domains, encompassing material characterization, nondestructive inspection, thermography, and biological analysis.[19–23] Nanocarbon materials, particularly carbon nanotubes (CNTs), have shown promise for long-wave infrared and THz sensing.[24–26] CNTs exhibit a broad absorption spectrum and flexibility, making them suitable for applications in infrared imaging, nondestructive evaluation, and chemical analysis under varying mechanical conditions.[25–29] However, earlier generations of CNT sensors relied on external equipment, limiting their efficiency, portability, and scanning speed.

Organic circuits constructed on organic thin-film transistors (OTFTs) stand out owing to their inherent flexibility and scalability. Consequently, they are an ideal choice for large-area imagers equipped with an active sensor matrix.[30–32] Such an active matrix design minimizes the number of wires and reduces crosstalk, enabling denser and faster sensor array readouts.[32] The versatility of these organic sensor matrices has been demonstrated in various fields, including temperature, pressure, and visible-light mapping.[30–36] With resolution specifications ranging from 1 to 50 dots per inch (dpi), they seamlessly fit into applications such as biosensing and soft robotics. Organic circuit components, such as voltage signal amplifiers, offer advanced signal processing capabilities.[37,38] These advantages of organic circuits position them as the foundation for pioneering CNT-based infrared imagers—an unexplored field (Table S1, Supporting Information). To realize this potential, it is crucial to increase the sensitivity of CNT sensors and enhance the stability of organic circuits under infrared irradiation.

In this study, a flexible imager tailored for large-area infrared imaging was developed using high-sensitivity CNT sensors and light-shielded OTFTs (**Figure 1**). When the CNT sensor was printed on a 2.4-µm-thick Parylene substrate, the output voltage increased by 21 times and the response speed was 15 times faster compared to sensors printed on thicker rigid substrates. This sensor maintained its efficacy even after being subjected to mechanical stresses such as bending and crumpling. The introduction of a light shield to the OTFTs ensured consistent performance during light irradiation, facilitating their use as reliable switching transistors within the imager. Furthermore, OTFTs were integrated as organic amplifiers, boosting THz detection signals by a factor of 10 while maintaining a low-noise profile. The flexible imager, equipped with an $8 \times 8$ CNT sensor matrix, demonstrated capability in sequential infrared imaging with wireless communication systems. Practical tests confirmed its utility for imaging heat sources, human hand, and in-solution glucose, highlighting the potential of infrared imaging in fields such as biochemistry and soft robotics.

Y. Kawano
National Institute of Informatics
2-1-2 Hitotsubashi, Chiyoda-ku, Tokyo 101–8430, Japan

## 2. CNT Sensors on Ultrathin Parylene Substrates

In this study, uncooled flexible CNT sensors were fabricated via dispenser printing. These sensors operate based on the photothermoelectric (PTE) effect exhibited by CNT films.[39] Upon irradiation with light, the CNT sensor absorbs light and heats up, creating a thermal gradient. This gradient generates a voltage signal in the CNT sensor, proportional to both the thermal gradient and the Seebeck coefficient.

A method to enhance sensitivity involves creating a heterogeneous interface within the CNT sensor, characterized by significantly different Seebeck coefficients. This was achieved by forming a p/n interface within the CNT sensor via chemical carrier doping using solutions of potassium hydroxide (KOH) and 15-crown-5-ether. Half of the CNT sensor was doped through dispenser printing of the solution. While the native CNT sensor exhibited p-type thermoelectric characteristics, the introduction of OH ions induced n-type thermoelectric properties. The voltage generated by the CNT sensor's PTE effect is expressed as

$$\Delta V = \left(S_{\text{p-type CNT sensor}} - S_{\text{n-type CNT sensor}}\right) \Delta T \quad (1)$$

where $S_{\text{p-type CNT sensor}}$ and $S_{\text{n-type CNT sensor}}$ represent the Seebeck coefficients for the p-type and n-type regions of the CNT sensor, respectively, and $\Delta T$ denotes the temperature gradient due to light irradiation. The Seebeck coefficients were investigated through voltage measurements with a temperature gradient of ≈5 °C. Figure S1, Supporting Information illustrates the changes in the Seebeck coefficients during the doping process. The Seebeck coefficients for the p- and n-type CNT films were 50 and −47 µV $K^{-1}$, respectively, in line with previous studies on CNT sensors (p-type: 45–50 µV $K^{-1}$, n-type: −40–−50 µV $K^{-1}$).[28,29]

An illustration of the CNT sensor after doping is shown in **Figure 2a**, which depicts a slightly whitened doped region. The smallest CNT sensors used in this study had dimensions of 2 mm × 0.4 mm and were formed on a 2.4-µm-thick Parylene substrate. Interferometry results (Figure 2b) indicated an increase in thickness and altered surface texture in the n-type region. Specifically, the thickness and surface roughness measured 0.92 and 0.19 µm, respectively, in the p-type region, compared to 1.1 and 0.47 µm, respectively, in the n-type region. Scanning electron microscopy (SEM; Figure S2, Supporting Information) showed bundles of CNTs in the p-type region and coating substances on the CNT films in the n-type region. This morphological change in the n-type region is likely attributable to the deposition of compounds from the doping solution.

To enhance sensitivity, an ultrathin Parylene polymer substrate with a thickness of 2.4 µm was chosen for the CNT sensors. The thermal conductivity of Parylene (diX-SR, obtained from Daisan Kasei Co.) is 0.13 W $m^{-1}$ $K^{-1}$, and its specific heat is 0.97 J $g^{-1}$ $K^{-1}$. A comparative study was conducted to assess the PTE response from CNT sensors on Parylene substrates of varying thicknesses: 2.4, 5, and 25 µm. Each substrate was created using chemical vapor deposition on a 1-mm-thick glass substrate, which had a thermal conductivity of 1.1 W $m^{-1}$ $K^{-1}$ and a specific heat of 0.77 J $g^{-1}$ $K^{-1}$.

The PTE response was determined by monitoring the voltage generated when a far-infrared (FIR) laser with a wavelength of 6.13 µm was directed through a 10-mm-long CNT sensor. As

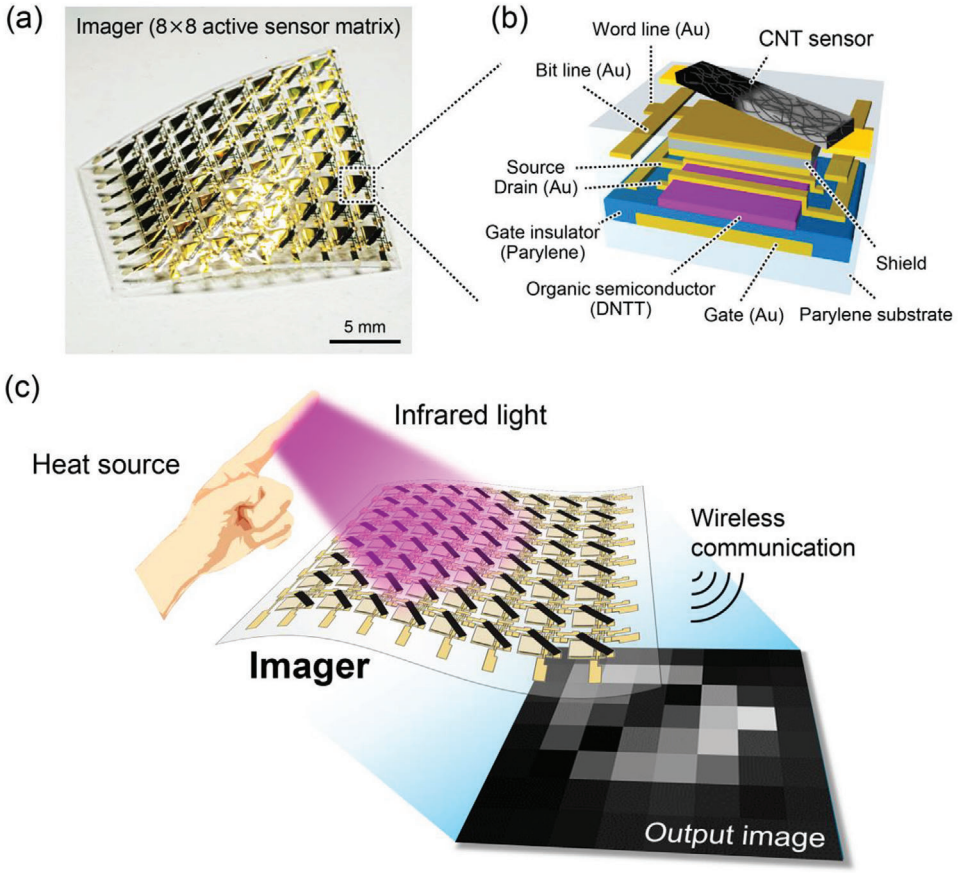


**Figure 1.** Flexible infrared imager integrated with CNT sensors and organic circuits. a) Imager featuring an 8 × 8 active matrix combined with CNT sensors and organic transistors. b) Schematic detailing a sensor cell within the imager, consisting of a CNT sensor paired with an organic transistor. c) Schematic illustrating thermal imaging through infrared detection, employing the imager in tandem with a wireless communication system.

Figure 2c illustrates, the PTE response peaked at the middle of the CNT sensor ($X$ = 0 mm), where the p/n interface was located, for all substrate types. The lowest response, 0.3 mV, occurred on the glass substrate, while the response on the 2.4-µm-thick Parylene substrate increased nearly 20-fold to 6.1 mV. To evaluate response speed, the time constant equivalent to 63.2% of the maximum response voltage was recorded when the FIR laser was applied near the p–n interface, the point of maximal response. As shown in Figure 2d, the CNT sensor on the glass substrate exhibited a delayed response, taking over 3 s for the voltage to stabilize. In contrast, the response times for CNT sensors on Parylene substrates of 2.4, 5, and 25 µm thicknesses were 201, 205, and 344 ms, respectively, indicating speeds up to 15 times faster than that on glass. These results, summarized in Figure 2e, confirm that both the PTE response and its speed are significantly enhanced by using an ultrathin Parylene substrate.

A thermal comparison between the 2.4-µm-thick Parylene substrate and the 1-mm-thick glass substrate revealed that their heat capacities per unit area were $2.2 \times 10^{-6}$ J mm$^{-2}$ K$^{-1}$ and $1.8 \times 10^{-3}$ J mm$^{-2}$ K$^{-1}$, respectively, while their sheet thermal resistances were $5.0 \times 10^{6}$ K W$^{-1}$ and $9.2 \times 10^{2}$ K W$^{-1}$, respectively. These findings confirm that the ultrathin substrate is better suited to concentrate heat generated by light irradiation due to its reduced heat absorption and lateral heat dispersion within the substrate, thus enhancing the photosensitivity of the CNT sensors.

The basic characteristics of the CNT sensor on 2.4-µm-thick Parylene substrates are presented in Figure S3, Supporting Information. These include the sensor's noise voltage and the noise equivalent power (NEP). The noise voltage of the CNT sensor, predominantly measured above 60 Hz and excluding the 50-Hz hum noise from the power supply, was estimated at ≈23 nV Hz$^{-1/2}$. This closely aligns with the theoretical estimation of thermal noise at 15 nV Hz$^{-1/2}$. The NEP was measured within a range of $10^{-12}$ W Hz$^{-1/2}$ for wavelengths spanning 660 nm to 10.3 µm. Additionally, the time constant was 47 ms for NIR light ($\lambda_{LED}$ = 870 nm) emitted from an LED source, as shown in Figure S4, Supporting Information. These NEP values and response times are comparable to those of conventional uncooled photodetectors.[15,40]

The effect of substrate materials on sensor performance was evaluated using polyimide, polyethylene naphthalate, and polyurethane elastomer films. All substrates had a uniform thickness of 25 µm, and their thermal characteristics are summarized in Table S2, Supporting Information. As illustrated in Figure S5, Supporting Information, CNT sensors were successfully formed on each polymer substrate. Their NEP and time constant were investigated using FIR light ($\lambda_{laser}$ = 6.13 µm).

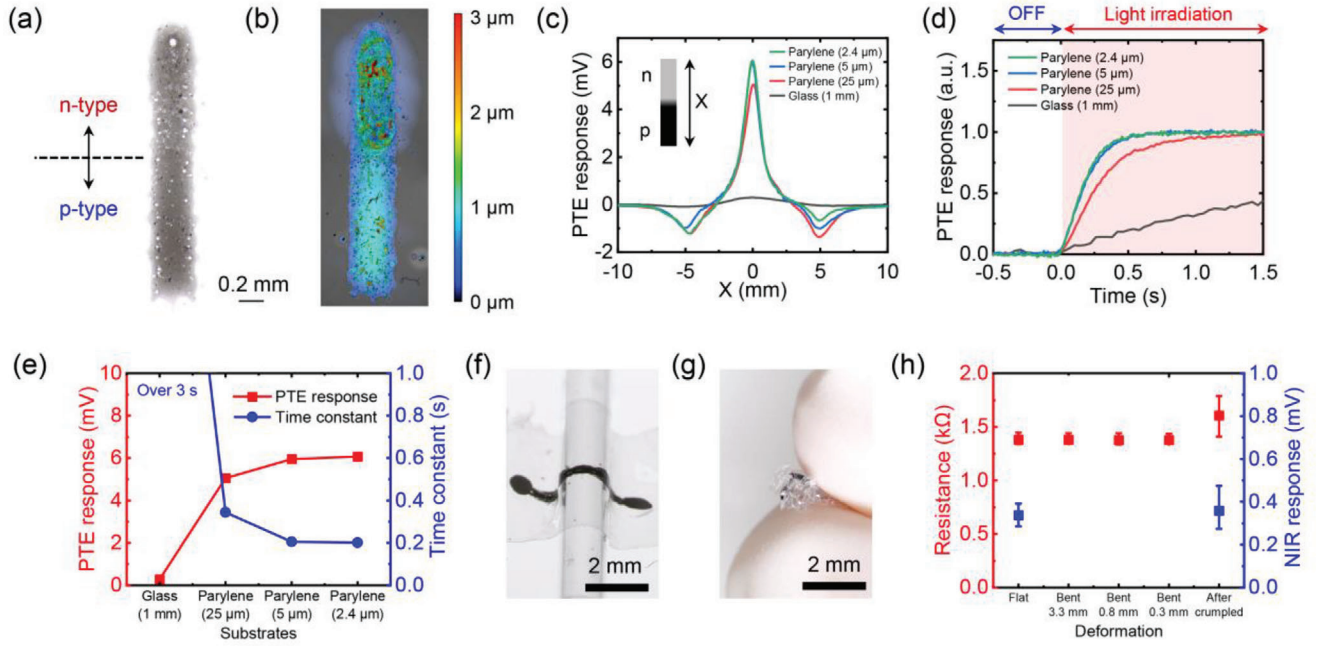


**Figure 2.** CNT sensor on ultrathin Parylene substrates. a) Image of a CNT sensor printed on Parylene substrates, with the dashed line indicating the p/n interface. b) Elevation mapping of the CNT sensor, visualized using white-light interferometry. c) Line profiles detailing the PTE response sourced along the length of a CNT sensor for substrates of different thicknesses. ($\lambda_{laser}$ = 6.13 μm) The inset shows the schematic axis direction of a CNT sensor. d) Temporal response patterns of CNT sensors subjected to FIR ($\lambda_{laser}$ = 6.13 μm) irradiation. e) Peak PTE response coupled with time-constant values for FIR ($\lambda_{laser}$ = 6.13 μm) irradiation. f) CNT sensor aligned with a 0.8-mm-radius probe. g) Crumpled CNT sensor. h) Variations in resistance and NIR ($\lambda_{LED}$ = 870 nm) response under diverse deformation conditions.

The NEP measurements fell within a range of $10^{-11}$ W $Hz^{-1/2}$, and the time constants were observed to be between 209 and 344 ms. While heat capacity and thermal resistance can influence the time constant and NEP, respectively, their effects were not pronounced. These results indicated that the CNT sensors maintained similar performance across all tested substrates.

CNT sensors possess a significant advantage of being adaptable to various substrates, including ultra-thin and flexible materials such as Parylene, stretchable materials like polyurethane elastomer film, general flexible substrates such as polyethylene naphthalate, and thermally stable substrates like polyimide. This adaptability offers the potential to enhance the performance of CNT sensors by optimizing the thickness of the polymer substrates. In particular, Parylene substrates provide the benefits of ultra-thin film formability down to a few micrometers and demonstrate large-area productivity for organic transistors and CNT sensors. Additionally, previous studies have shown that the geometry and thermal properties of PTE sensors and substrates can affect their sensitivity and response time.[41,42] Our study extends previous knowledge by investigating various flexible substrates and printed CNT sensors and examining their effects on sensor responses.

To assess the mechanical flexibility of CNT sensors on 2.4-μm-thick Parylene substrates, we analyzed changes in resistance and NIR response under various deformations. The sensors were bent with curvature radii ranging from 3.3 to 0.3 mm, as depicted in Figure 2f, and were also subjected to crumpling (Figure 2g). The behavior of the CNT sensors under these conditions is detailed in Figure S6, Supporting Information. Each deformation test, from bending to crumpling, was performed on the same sample. Figure 2h shows that the resistance changes were minimal across all bending manipulations, with a deviation of less than 0.2%. After crumpling, resistance increased by 24%, while the average fluctuation in NIR response was ≈7.0%. Additionally, the cyclic bending durability of CNT sensors with a bending radius of 0.68 mm was investigated. As illustrated in Figure S7, Supporting Information, the changes in photoresponse were only 14% after 1000 bending cycles. Therefore, the CNT sensors on ultrathin Parylene substrates exhibited considerable stability under substantial mechanical distortions, including bending and crumpling.

## 3. Organic Transistor with Light Shield for Stable Operation of Imager

The organic circuits were composed of OTFTs using dinaphtho[2,3-b:2′,3′-f]thieno[3,2-b]thiophene (DNTT) as a p-type organic semiconductor, paired with a Parylene gate dielectric ≈50 nm thick. These OTFTs were fabricated on 2.4-μm-thick Parylene using the shadow mask technique, resulting in a device with an overall thickness of 3.7 μm. The OTFT structure featured a bottom-gate, top-contact design, as illustrated in **Figure 3a**. For imager applications, it is crucial that OTFTs maintain stable characteristics under light irradiation.[43,44] To achieve this, 180-nm-thick metal films were deposited directly over the OTFT channels, serving as shields against both visible and infrared light. This shielding structure was comprised of three metallic

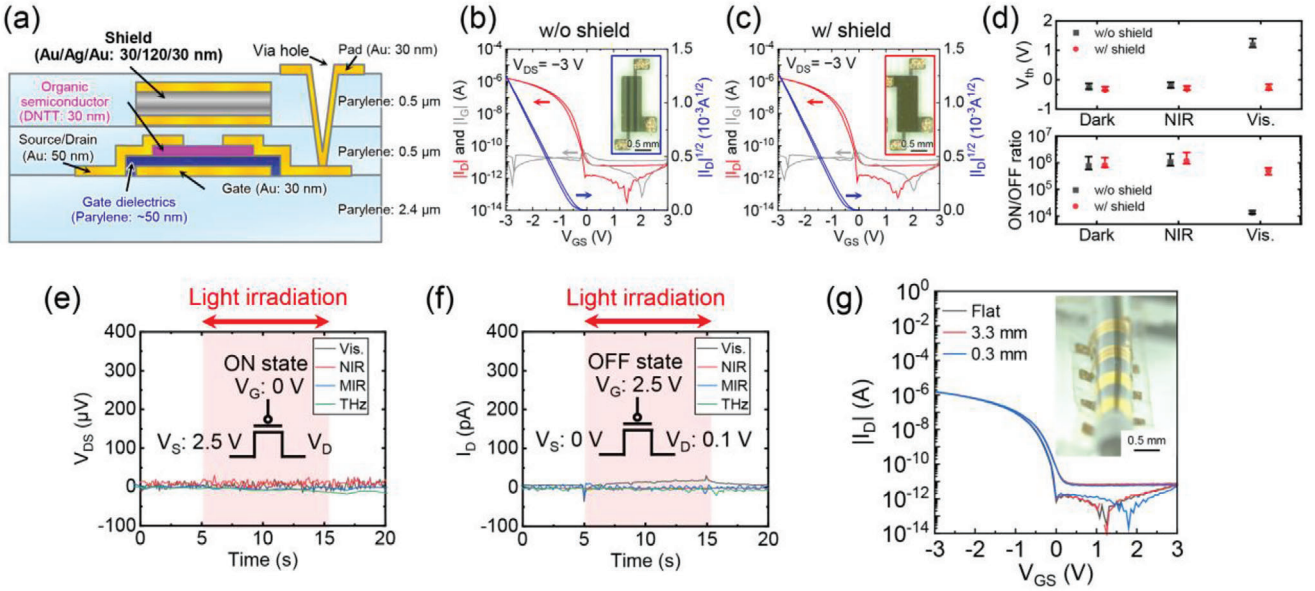


**Figure 3.** Shielded OTFTs. a) Lateral diagram of shielded OTFTs. Transfer curves for OTFTs b) without and c) with shielding. The insets show overviews of the OTFTs. d) Changes in $V_{th}$ and the ON/OFF ratio of OTFTs with and without shielding, examined under dark conditions and during NIR ($\lambda_{LED}$ = 870 nm) and visible-light (vis.) irradiation ($\lambda_{LED}$ > 400 nm). e) $V_{DS}$ response of the shielded OTFT in the ON state ($V_{GS}$ = −2.5 V) during varied light irradiation. The light sources were vis. ($\lambda_{LED}$ > 400 nm), NIR ($\lambda_{LED}$ = 870 nm), MIR ($\lambda_{laser}$ = 4.33 μm), and THz ($\lambda_{laser}$ = 577 μm). Insets depict the activated switching OTFT. f) Drain current ($I_D$) response of the shielded OTFT in the OFF state ($V_{GS}$ = 2.5 V) during varied light irradiation. Insets illustrate the deactivated switching transistor. g) Transfer curves of OTFTs in a flat state (black) and when bent at radii of 3.3 mm (red) and 0.3 mm (blue). The inset displays the OTFTs along a probe with a 0.3-mm radius.

films: Au (30 nm), Ag (120 nm), and an additional Au layer (30 nm).

To evaluate the effectiveness of the light-shielding mechanism, the light transmittance of the 180-nm-thick metal film was examined using ultraviolet–visible (UV–vis) spectroscopy ($\lambda$ = 200–1000 nm), Fourier transform infrared (FT-IR) spectroscopy ($\lambda$ = 1.4–6.6 μm), and THz time-domain spectroscopy (THz-TDS; $\lambda$ = 167 μm–2 mm). As depicted in Figure S8, Supporting Information, the shield's light transmittance was ≈0% across all examined wavelength spectra. This indicated that the 180-nm-thick metallic shield effectively blocked incoming light, reducing its incidence on the channel. These results are in line with previous research, which suggests that metal films exceeding 100 nm in thickness possess reflective and attenuative properties over a broad wavelength range, extending from visible to THz wavelengths.[45,46]

Figure 3b,c, along with Figure S9, Supporting Information, displays the transfer and output curves of OTFTs with a channel width-to-length ratio ($W/L$ ratio) of 15 ($W/L$ = 1.5 mm/0.1 mm). The parameters derived from the transfer curves of 12 unshielded OTFTs were as follows: an average mobility ($\mu$) of 0.48 $cm^2\ V^{-1}\ s^{-1}$ with a standard deviation (SD) of 0.030 $cm^2\ V^{-1}\ s^{-1}$, an average threshold voltage ($V_{th}$) of −0.35 V with an SD of 0.047 V, and an ON/OFF ratio exceeding $10^5$. The shielded OTFTs exhibited (averages from 12 devices) $\mu$ = 0.48 $cm^2\ V^{-1}\ s^{-1}$ with an SD of 0.028 $cm^2\ V^{-1}\ s^{-1}$, $V_{th}$ = −0.52 V with an SD of 0.029 V, and an ON/OFF ratio greater than $10^5$. These results indicate that the shielded OTFTs maintain similar characteristics to their unshielded counterparts. Additionally, the shielding can function as a double gate for the OTFTs, modulating the $V_{th}$ through electrical potential control.[47,48] Although the OTFTs were assessed in a floating state, where the shield potential remained unfixed, the characteristics of the OTFTs with a floating shield mirrored those observed when the shield voltage was set at 0 V (as shown in Figure S10, Supporting Information).

Figure 3d illustrates the variations in $V_{th}$ and the ON/OFF ratio, derived from the transfer curves (shown in Figure S11, Supporting Information), during light irradiation. Both $V_{th}$ and the ON/OFF ratios under NIR irradiation ($\lambda_{LED}$ = 870 nm) closely matched those in a dark environment, even for unshielded OTFTs. However, under visible light irradiation, the unshielded OTFTs exhibited a positive shift in $V_{th}$ of 1.4 V, and the ON/OFF ratio decreased to 1.8%. In shielded OTFTs, this shift in $V_{th}$ was negligible, and the reduction in the ON/OFF ratio was limited to 60%. Moreover, visible-light irradiation influenced the drain current ($I_D$), with its effects being mitigated by over 90% in shielded OTFTs, as demonstrated in Figure S12, Supporting Information. The changes in characteristics due to visible light are attributed to photocarrier excitation.[49,50] Considering that the optical bandgap of DNTT is ≈3.0 eV, it absorbs light with a wavelength of ≈400 nm (3.1 eV).[51] Therefore, the shielding's role is crucial in minimizing the penetration of visible light into the channel, effectively reducing the shifts in $V_{th}$ and the ON/OFF ratio.

To further investigate the effects of light irradiation on the switching behavior of OTFTs, shielded OTFTs were subjected to varying light conditions while maintaining the operating parameters of a switching transistor. The changes in drain-source voltage ($V_{DS}$) in its ON state (gate-source voltage $V_{GS}$ = −2.5 V) and

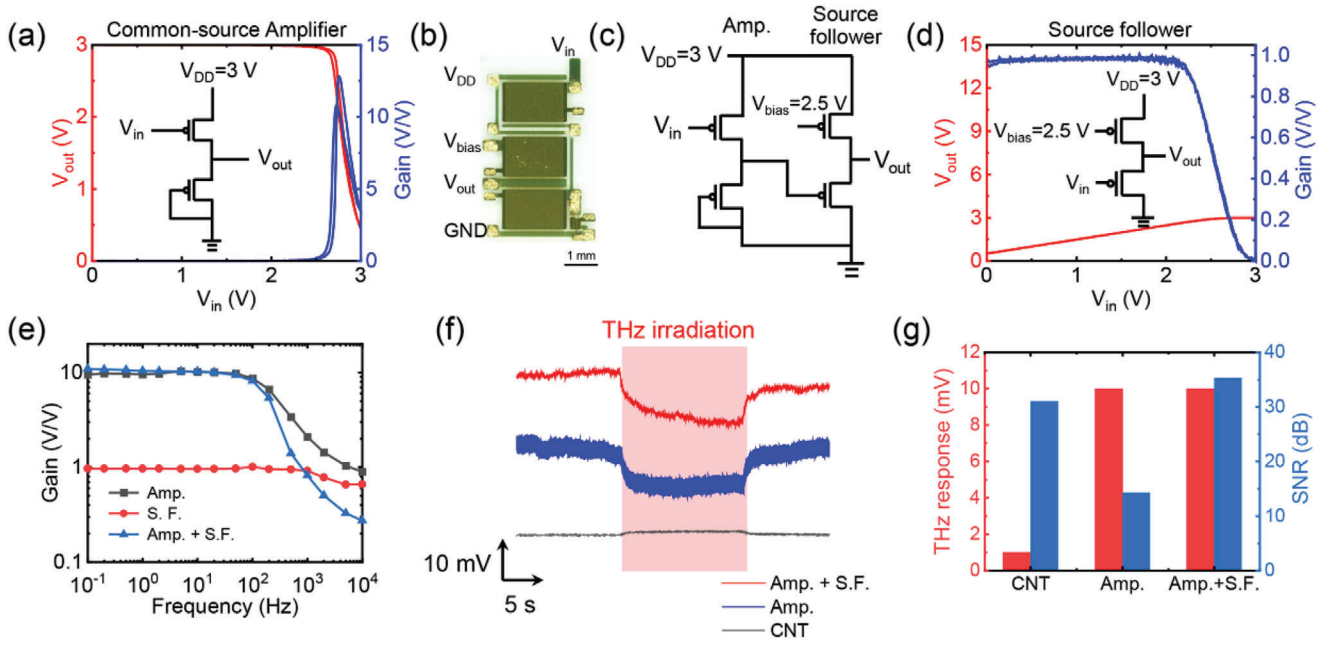


**Figure 4.** Organic voltage amplifiers tailored for enhanced THz detection. a) Common-source amplifier response and associated gain characteristics, with an inset depicting the OTFT-based common-source amplifier circuit diagram. b) Image and c) circuit diagrams of the common-source amplifier combined with a source follower using OTFTs. d) Source-follower response and its gain characteristics, with the inset showing its circuit diagram. e) Gain characteristics of the common-source amplifier and source follower with respect to the frequency. f) Temporal responses to THz ($\lambda_{laser}$ = 577 nm) detection signals from the CNT sensor, the common-source amplifier, and the combined unit of the common-source amplifier paired with a source follower. g) Responses to THz ($\lambda_{laser}$ = 577 nm) irradiation alongside the signal-to-noise ratio (SNR) for various signals.

drain current ($I_D$) fluctuations in its OFF state ($V_{GS}$ = 2.5 V) were evaluated. The employed light sources encompassed visible light (from a white LED), NIR (870 nm), mid-infrared (MIR; 4.33 µm), and THz (577 µm) irradiation. Figure 3e presents the $V_{DS}$ readings of the switching transistor in its ON state, measured under conditions where source voltage ($V_S$) and gate voltage ($V_G$) were fixed at 2.5 and 0 V, respectively, as depicted in the accompanying inset. The results demonstrate that $V_{DS}$ remained stable across all wavelengths of light irradiation, confirming the capability of the shielded OTFTs to consistently relay voltage signals while functioning as ON-state switching transistors. To evaluate the $I_D$ of shielded OTFTs in the OFF state, $V_S$, drain voltage ($V_D$), and $V_G$ were adjusted to 0, 0.1, and 2.5 V, respectively. As illustrated in Figure 3f, minimal $I_D$ deviations were observed under NIR, MIR, and THz irradiation. The most significant $I_D$ alteration occurred under visible light, with a peak $I_D$ of ≈36 pA. However, the ON/OFF ratio remained higher than $10^5$, considering the $I_D$ (≈8.6 µA) of the ON state (with $V_{GS}$ = −2.5 V and $V_{DS}$ = 0.1 V). These observations are attributed to the consistent behavior of the shielded OTFTs under various light conditions, indicating their suitability as switching transistors within the active matrix of imagers.

The mechanical flexibility of shielded OTFTs was evaluated through a bending assessment. The OTFTs were conformed to cylindrical surfaces and their performance was analyzed via transfer curves recorded during bending. The design of the shielded OTFTs strategically positioned the neutral-plane near the channel to facilitate stress relaxation during bending, as shown in Figure S13, Supporting Information. Both the channel layer and the neutral stress position of the OTFTs were ≈2.5 µm from the base. Transfer curves of the shielded OTFTs, obtained both in a flat state and under bending radii of 3.3 and 0.3 mm (Figure S3g, Supporting Information), showed consistent performance across various bending radii. $I_D$ and $I_G$ values derived from these transfer curves at $V_{GS}$ = $V_{DS}$ = −3 V are depicted in Figure S14, Supporting Information. Notably, even at the smallest bending radius of 0.3 mm, the shifts in $I_D$ and $I_G$ remained below 8%. The cyclic bending durability of the shielded organic transistors with a bending radius of 0.39 mm was also examined. These transistors maintained stable characteristics, exhibiting a change of less than 25% even after 1000 bending cycles (Figure S15, Supporting Information). These findings indicate that mechanical deformation had a negligible impact on the electrical properties of the shielded OTFTs.

## 4. Organic Voltage Amplifiers for Enhanced THz Detection of Single CNT Sensors

Organic voltage amplifiers were developed to augment infrared light detection via CNT sensors, which exhibit relatively low voltage responses (typically in the millivolt to microvolt range). Addressing the challenge of noise mitigation and isolation in optical measurement environments remains crucial for detecting such weak signals. Typically, this involves integrating external circuits and employing optical modulation. Organic amplifiers offer a practical solution. Utilizing two OTFTs, a diode-loaded common-source amplifier was constructed, as depicted in the schematic inset of **Figure 4a**. The $W/L$ ratios of the input and load transistor channels were 4286 (60 000 µm/14 µm) and 4 (200 µm/50 µm), respectively. As shown in Figure 4a, this common-source

amplifier achieved a gain peak of up to 12.7 times with an input voltage of 2.8 V. The output impedance of the amplifier is analogous to the resistance of the load transistor, which is determined from the current–voltage (*I–V*) characteristics of the diode-connected transistor. At maximum gain, the output voltage of the amplifier was ≈2 V, which corresponds to the operational voltage of the diode-loaded transistor. The output impedance of the amplifier circuit, estimated at ≈6 MΩ based on the gradient of the *I–V* characteristics around the 2-V mark (Figure S16a, Supporting Information), is crucial for reducing external noise and improving the signal-to-noise ratio (SNR). However, common-source amplifiers involve a trade-off between lowering output impedance and maximizing gain.

To reduce the output impedance while maintaining the desired gain, a source-follower circuit integrated with OTFTs was appended to the subsequent stage of the common-source amplifier, as shown in Figure 4b,c. The source follower was configured with two OTFTs, each having a channel $W/L$ ratio of 4286 (60 000 µm/14 µm). As depicted in Figure 4d, when the $V_{bias}$ was set to 2.5 V, the source follower relayed signals with an approximate onefold gain over the input voltage range of 0–2.2 V. The output impedance inherent to a source follower is the inverse of the input transistor's transconductance ($g_m^{-1}$), which can be inferred from the transfer curves of the OTFT in its saturation region (refer to Figure S16b, Supporting Information). The source follower's input voltage is ≈2 V, corresponding to the peak output voltage of a common-source amplifier. This implies that when the input voltage is 2 V, as shown in Figure 4d, the source follower's output voltage is ≈2.5 V, resulting in a $V_{GS} = V_{in} - V_{out}$ value of ≈−0.5 V for the input transistor. Therefore, the estimated output impedance for the source-follower circuit, at approximately $V_{GS}$ = −0.5 V, is 149 kΩ. These results suggest that integrating the source follower can reduce the amplifier's output impedance by a factor of ≈0.024.

Figure 4e illustrates the frequency behaviors of the organic amplifiers. The cutoff frequencies for the common-source amplifier and the source follower were above 200 Hz and 2 kHz, respectively. However, when the common-source amplifier was coupled with the source follower, the cutoff frequency ranged between 100 and 200 Hz, indicating a slight decrease compared to the standalone common-source amplifier. This behavior is primarily due to signal attenuation resulting from the common-source amplifier's output impedance and the source follower's input capacitance. Conversely, considering that the CNT sensor's time constant was 47 ms, the organic amplifiers exhibited a response rate that can follow the speed of CNT signals.

The efficiency of the proposed organic amplifiers in amplifying THz detection signals was evaluated. As depicted in Figure S17, Supporting Information, the CNT sensor was connected to the input of the organic amplifier using a direct current (DC) bias voltage and then exposed to THz light for 20 s. Figure 4f shows the output signals from the CNT sensor, the common-source amplifier, and the combined unit of the common-source amplifier paired with a source follower. The amplitude and SNR of this output signal, as derived from the temporal responses, are illustrated in Figure 4g. Under THz irradiation, the CNT sensor's output was 1 mV, with an SNR of ≈31 dB. When processed through the common-source amplifier, the signal was amplified tenfold to ≈10 mV. However, the output signal was affected by 3.6-mV hum noise (50 Hz), leading to a reduction in SNR to 14 dB, which was 17 dB lower than that of the independently measured CNT sensor.

Interestingly, the integration of a source-follower circuit with the common-source amplifier yielded an outcome similar to the tenfold amplification observed with the common-source amplifier alone. Additionally, the amplitude of the hum noise decreased to 0.11 mV, marking a substantial reduction to 0.029 times that of the common-source amplifier circuit alone. This reduction correlated well with the output-impedance ratio of the source follower to the common-source amplifier, which was 0.024. Consequently, the amplified signal's SNR increased to 35 dB, achieving a 4-dB enhancement compared to the standalone CNT sensor.

## 5. Active Sensor Matrix for Infrared Imager

Building on prior research advancements, an imager integrated with an active matrix of CNT sensors and OTFTs was developed for large-area infrared imaging, as shown in **Figure 5a**. The sensor cell of the imager, detailed in Figure 5b, consists of a CNT sensor and a switching OTFT. These components are sequentially connected to control the signal from the CNT sensor. With an ON voltage of −2.5 V applied to the word line (WL), the sensor signal is conveyed to the bit line (BL); when an OFF voltage of 2.5 V is applied to the WL, the sensor is disconnected. The active matrix is composed of 8 rows and 8 columns, totaling 64 elements. Each sensor cell occupies an area of 2.2 × 2.2 $mm^2$, resulting in a total imager area of 310 $mm^2$ and a resolution of 11.5 dpi. Signals from the eight BLs are processed by analog-to-digital (A/D) converters for each line, and the processed data is wirelessly transmitted to a computer for the generation of standardized images in 256 steps (Figure S18, Supporting Information).

The implemented active matrix integrates shielded OTFTs with a channel $W/L$ ratio of 2143 (30 000 µm/14 µm). The distribution of mobility is shown in Figure 5c,d, and the $V_{th}$ and ON/OFF ratios for the 63 operational OTFTs are presented in Figure S19, Supporting Information. A single OTFT malfunctioned due to gate dielectric leakage. However, this OTFT was electrically isolated and did not affect the other sensor cells connected to the same WL and BL. The average mobility was measured at 0.29 $cm^2\ V^{-1}\ s^{-1}$, with an SD of 0.011 $cm^2\ V^{-1}\ s^{-1}$, and the average $V_{th}$ was determined to be −0.59 V, with an SD of 0.027 V. All OTFTs exhibited ON/OFF ratios of $> 10^6$. The CNT sensor, measuring 2 mm in length and 0.4 mm in width, was placed on a 2.4-µm-thick Parylene substrate in the active matrix.

To evaluate the imager's optical sensitivity, the noise voltage and NEP of the CNT sensor were examined when paired with the switching OTFT. Figure S20a, Supporting Information shows the circuit layout used for measuring noise voltage; here, both the CNT sensor and switching OTFT are connected in their ON states ($V_{GS}$ = −2.5 V). The detected noise voltage was ≈0.24 µV $Hz^{-1/2}$, representing an ≈10.8-fold increase compared to a standalone CNT sensor (as shown in Figure S20b, Supporting Information). Given that the CNT sensor in the imager was on a 2.4-µm-thick Parylene substrate, its photoresponse was similar to that of an individual CNT sensor. Consequently, the NEP was found to increase by a factor of ≈10.8, due to its direct proportionality to the noise voltage. The value was calculated to

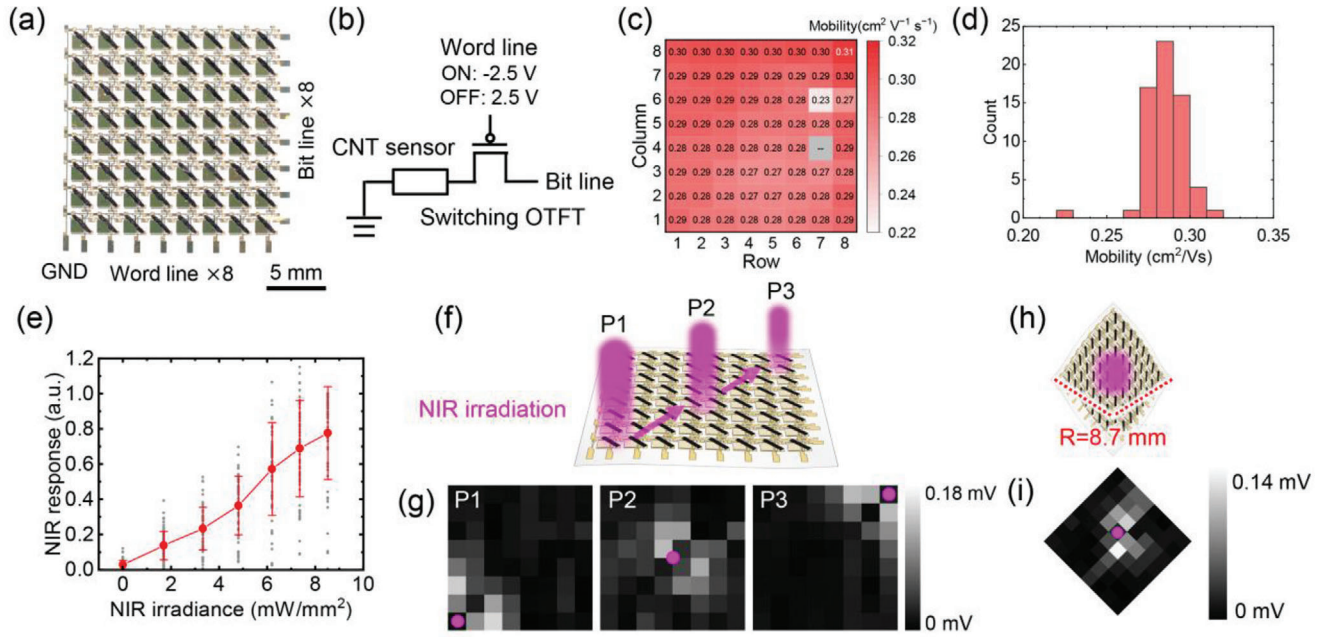


**Figure 5.** Infrared imager integrated with an active matrix consisting of CNT sensors and OTFTs. a) Detailed view of the imager incorporating CNT sensors and switching OTFTs. b) Circuit diagram of an individual sensor cell. c) Mobility spread of an 8 × 8 OTFT matrix and d) a histogram for 63 of the 64 OTFTs. e) Correlation between the imager's output and NIR irradiance ($\lambda_{LED}$ = 870 nm). The gray points and error bars in the data represent the collective dataset and the SD, respectively. f) Schematic and g) output images following a singular NIR light's dynamic irradiation ($\lambda_{LED}$ = 870 nm), with a pink circle marking the core of the exposed region. h) Depictions of the imager bent at a radius of 8.7 mm and i) output following NIR irradiation ($\lambda_{LED}$ = 870 nm), with the pink circle pinpointing the core of the exposed zone.

be $10^{-11}$ W $Hz^{-1/2}$ within the wavelength range of 660 nm to 10.3 µm. (Figure S20c, Supporting Information). Although the connection to the switching OTFT slightly degraded the NEP, the resultant performance remained comparable to that of traditional uncooled infrared detectors.[15,40] Sensitivity can be further enhanced by integrating organic amplifiers, a topic that will be addressed in the discussion.

The correlation between the energy of the incoming light and the brightness of the output image was investigated. The light source used was large-area NIR light, substantially larger than the imager. The output voltages were normalized to the peak voltage observed at an irradiation intensity of 8.5 mW $mm^{-2}$, and the SD error bars are presented in Figure 5e. Furthermore, Figure S21, Supporting Information displays images captured at various irradiance levels ranging from 0 to 8.5 mW $mm^{-2}$. The average output of the imager was generally directly proportional to the energy density of NIR irradiance, enabling quantitative irradiance evaluation. Variations in brightness across several pixels were attributed to the differing photosensitivity of the CNT sensors, with a peak SD of 0.27 at an irradiation level of 7.4 mW $mm^{-2}$. The optimization of device design can help to reduce variability, which will be explored in the discussion.

Imagers integrated with active arrays of CNT sensors enable continuous and extensive infrared imaging. In this experiment, a solitary NIR light source was projected onto the imager, and the movement of this light was recorded. The NIR source moved across the imager, following the trajectory indicated by the arrow in Figure 5f (from P1 to P3). The imager was set to output images at a rate of 1.3 Hz, and a sequence of these images is presented in Figure 5g. Due to the low directivity of the LEDs, multiple pixels responded to the NIR irradiation. The illuminated pixels represent the areas receiving irradiation, and their changing positions, as the light source moved, enabled the capture of dynamic NIR irradiation events. Video S1, Supporting Information offers a dual perspective: the left side depicts the NIR irradiation on the imager, while the right side features a compilation of sequential output images. The movements of the NIR irradiation and the illuminated sections of the imager's output video are synchronized both spatially and temporally. Additionally, Figure 5h and Figure S22, Supporting Information show the imager bent to a bending radius of 8.7 mm, and Figure 5i displays the corresponding output image. Video S2, Supporting Information demonstrates a series of output images produced by the bent imager. In these demonstrations, the NIR-irradiated zones precisely correspond with the illuminated regions in the output images, confirming the effective functionality of the imager in both bent and flat states.

## 6. Broadband Infrared Imaging for Thermal and Biochemical Analysis

In this study, the ability of the imager to capture various heat sources was evaluated to determine its potential for thermal imaging. Thermal radiation involves the emission of electromagnetic waves, predominantly in the form of MIR and FIR light, particularly at ambient temperatures. Imagers with CNT sensors exhibit heightened sensitivity to infrared light, making them promising for passive thermal and biochemical

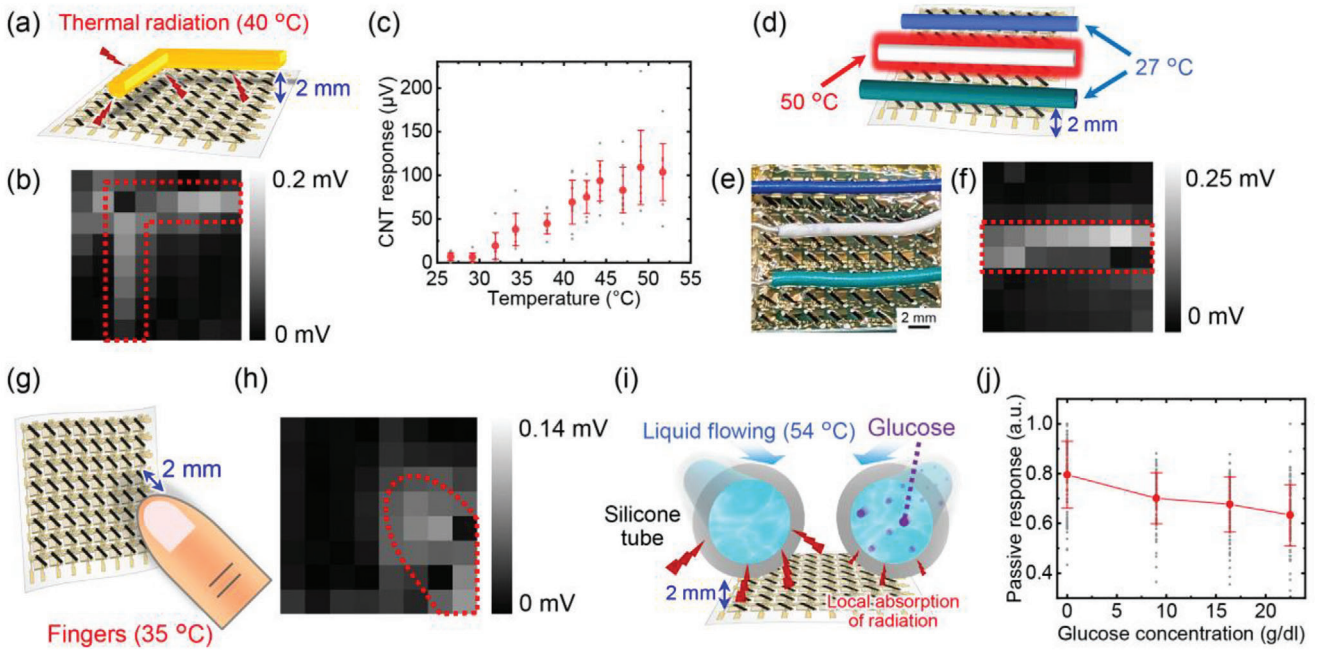


**Figure 6.** Broadband infrared detection-based thermal imaging. a) Schematic and b) resultant image of an L-shaped wire heated to 40 °C; the red dashed area aligns with the wire's configuration. c) Correlation between the imager's output and the temperature of the wire. The gray points and error bars in the data represent the collective dataset and the SD, respectively. d) Conceptual representation, e) photograph, and f) matching output image of a wire heated to 50 °C (illustrated in white), flanked by unheated wires at 27 °C (displayed in blue and green), where the red dashed area specifies the heated wire's position. g) Conceptual sketches of a 35 °C human finger placed over the imager. h) Output captures of the aforementioned finger, with a red dashed line denoting its position. i) Conceptual representation of glucose detection in a circulating solution. The liquid was heated to 54 °C, and its thermal radiation was reduced by glucose absorption. j) Correlation between the imager's output and the glucose solution's concentration. The gray points and error bars in the data represent the collective dataset and the SD, respectively.

visualizations. **Figures** 6a and S23a, Supporting Information display an L-shaped wire made of polyvinyl chloride (PVC)-coated tinned Cu heated to ≈40 °C (as shown in Figure S23b, Supporting Information). This wire was positioned 2 mm from the imager. The resulting images successfully captured the wire's shape, with the distinct vertical and horizontal segments of the L-shape evident in the output image (Figure 6b). The image in Figure S23c, Supporting Information shows both the imager and a straight wire, which was bent to a curvature of 8.7 mm. This confirms the imager's capability to accurately visualize the heated wire in both bent and flat configurations (as depicted in Figure S23d, Supporting Information). Figure 6c illustrates the correlation between the imager's output and the temperature of the heated wire. With an ambient temperature of ≈27 °C, the imager effectively detected thermal radiation from sources with temperatures above 32 °C. Remarkably, the output's average value showed an almost linear relationship with temperature, enabling quantitative thermal imaging.

The imaging response to a thermal source is predominantly influenced by the absorption of infrared emissions from thermal radiation. To elucidate this mechanism, a black polypropylene (BPP) film, which allows the transmission of light with wavelengths above 5 μm, was positioned between the heated straight wires (at 50 °C) and the imager, as depicted in Figure S24a,b, Supporting Information. This placement of the BPP film was crucial for impeding convective heat transfer toward the imager and minimizing atmospheric thermal dispersion, thereby ensuring that the imaging conditions were primarily governed by thermal radiation. The discernibility of the wire configuration in the output image through the BPP film, as shown in Figure S24c, Supporting Information, confirms that thermal imaging was effectively conducted via the detection of infrared light with wavelengths greater than 5 μm. Furthermore, Figure S25, Supporting Information demonstrates the consistent infrared detectivity of the CNT sensor across ambient temperatures ranging from 23 to 100 °C, highlighting its applicability for thermal analysis at elevated temperatures.

To demonstrate the thermal detection capability, wires subjected to various temperatures—indistinguishable under visible light conditions—were imaged. Figure 6d,e depicts three coated wires positioned 2 mm above the imager. The central white wire was heated to ≈50 °C via Joule heating, while the surrounding green and blue wires remained at room temperature, ≈27 °C. The imager's output, as shown in Figure 6f, displayed brightness solely in the center, indicating the location of the heated wire. Images taken under identical experimental conditions, with wires oriented both diagonally and vertically, are shown in Figure S26, Supporting Information. Moreover, several wires at different temperatures of 40 and 60 °C were detected successfully (Figure S27, Supporting Information). The proficiency of the imager in imaging heat sources is emphasized by these results.

The imager's high thermal sensitivity facilitates the visualization of thermal emissions from the human body, which, in accordance with Planck's law, predominantly comprises infrared

light with a peak wavelength of ≈9.5 µm.[52] A human finger, with a surface temperature of ≈35 °C, was positioned 2 mm away from the imager, as depicted in Figure 6g. The resulting output (Figure 6h) revealed bright pixels coinciding with the region where the finger and the imager overlapped. Video S3, Supporting Information sequentially presents the imaging process; the movements of the finger correspond to the illuminated section of the output video, indicating effective capture of biological motion.

To demonstrate the imager's utility in biochemical analysis, it was employed for the detection of liquid glucose. The experimental setup is illustrated in Figure 6i. The solution, maintained at a constant temperature, circulated through a silicone tube, with glucose concentrations ranging from 0 to 23 g $dl^{-1}$. The introduction of glucose into this solution attenuated thermal radiation due to localized absorption by the dissolved glucose. The imager, positioned 2 mm below this tubing, enabled assessments of glucose concentration based on its output. With the solution's temperature stabilized at 54 °C through a water bath, the inverse relationship between glucose concentration and imager output was examined, as shown in Figure 6j. As glucose concentration increased, the imager's output typically decreased. This observation confirms the imager's potential for noninvasive, label-free evaluations of liquid-based chemicals, stemming from its high sensitivity to thermal radiation.

## 7. Discussion

Owing to the broad distribution observed in the output data of the imager, it is essential to enhance the quality of imaging. Previous studies have shown that high-quality CNT sensors (created through filtration rather than printing) enable the generation of a relatively accurate calibration curve for measuring infrared light. Additionally, CNT sensors fabricated by filtration and doped via droplet injection have been specifically chosen for their superior analytical quality in temperature and glucose assessments.[29] The response accuracy of the printed and selected CNT sensors to visible light (625 nm; red) and NIR light (870 nm) was examined. As indicated in Figure S28a,b, Supporting Information, the responses were proportional to the intensity of the light sources, and their dispersion was markedly reduced when normalized by the maximum value for each sensor. The normalized responses to heated wires (25–186 °C) were also proportional to the wire temperatures, displaying minimal variation (Figure S28c, Supporting Information). This normalization approach, based on each sensor's maximum value, effectively reduces dispersion, thereby enhancing measurement precision. Consequently, the imager holds promise for applications such as photoplethysmography owing to its quantitative detectivity of red and NIR light and a response speed exceeding 10 Hz.[53]

Some pixels in the infrared and thermal imaging exhibited a lack of response to light, adversely affecting image quality. This unstable photoresponse is ascribed to light diffusion and the multiple PTE effects in the CNT sensor. An investigation was conducted to understand the relationship between the irradiation position and the sensor's response. As depicted in Figure S29a, Supporting Information, an NIR LED was positioned 2 mm above a CNT sensor and moved from the sensor's center. As shown in Figure S29b, Supporting Information, the responses remained even when the LED was 10 mm from the sensor along the Y-axis. Moreover, there are two types of light responses: the peak response for the CNT sensor 1 occurred at 0 mm, while that of CNT sensor 2 occurred at 3 mm. This phenomenon is attributed to light diffusion and multiple PTE responses arising from three interfaces: the boundary between two types of CNT films ($S_{\text{p-type CNT film}} = 50$ µV $K^{-1}$, $S_{\text{n-type CNT film}} = -47$ µV $K^{-1}$), and the interface between the CNT and electrode ($S_{\text{electrode}} = 1.5$ µV $K^{-1}$) at both sensor ends. Figure 2c corroborates this effect, showcasing the response of a 10-mm-long CNT sensor to a sweeping focused FIR laser (spot size of 3 mm, $\lambda = 6.13$ µm). The maximum response was observed at the center of the CNT sensor, while the light response diminished or became negative when the light irradiated the ends of the sensor ($X = 5$ and $-5$ mm). Therefore, when the diffused LED is centered over the CNT sensor, a mild thermal gradient is formed across the sensor, leading to a neutralization of the PTE response at the center by inverse PTE responses at the ends. Conversely, with the LED positioned 3 mm from the center along the Y-axis, the light irradiation on the metal-CNT interface is minimized, yielding the strongest PTE response at the center.

The ratio of the light-exposed area to the CNT sensor size also has a significant effect on the response. Figure S29c, Supporting Information shows the time response of the 2- and 10-mm-long CNT sensors for the NIR LED irradiation. There are response attenuations after light irradiation for the 2-mm-long CNT sensor, resulting in responses of approximately less than 80 µV. In contrast, the 10-mm-long CNT sensor showed a stable and large response of ≈800 µV. The size dependence for NIR LED irradiation is summarized in Figure S29d, Supporting Information; the response was improved when the CNT sensor was longer than 5 mm. These results indicate that the light response can be enhanced when the light is irradiated only at the center of a CNT sensor, except for the interface between CNT sensors and electrodes. To demonstrate this, we incorporated a light shield layer at the sensor's ends, as shown in Figure S29e, Supporting Information. A 1.5-fold improvement in response was demonstrated when an NIR expanded laser was directed onto a CNT sensor equipped with end shields (Figure S29f, Supporting Information). This method is desirable to improve the response of small CNT sensors required for the imager.

In this study, a substantial quantity of CNT sensors was simultaneously printed and doped on a large-area substrate. Given this process, it is challenging to selectively choose CNT sensors post-fabrication as their formation largely depends on variations inherent in the printing technique. Nevertheless, the accuracy of measurements for infrared light, temperatures, glucose, and other parameters can be improved by adjusting and homogenizing the PTE response. This is achievable using end shields, the effectiveness of which is detailed in Figure S29f, Supporting Information. Future research should focus on exploring detailed structures and material formulations with the aim of minimizing variations in sensor characteristics following large-area and printable fabrication. This approach is essential for enhancing the consistency and reliability of CNT sensors produced on a large scale.

Organic active matrices play a crucial role in enabling our flexible imager to achieve large-area sequential image capturing. When CNT sensors operate independently, both wire and channel counts increase significantly, leading to a decline in

CNT sensor sensitivity due to an increased thermal capacitance inherent in the substrate. Furthermore, traditional passive arrays that rely on blocking diodes are primarily restricted to photodiodes[54,55] and are not suitable for CNT sensors that convert light to voltage by the PTE effect. The demonstrated organic active matrix represents a promising technology for overcoming these limitations and achieving large-area imaging. Moreover, the fabrication of this active matrix incorporates scalable printing and deposition techniques, highlighting its scalability. This method facilitates the generation of large-area matrices through simple circuit structure extensions. The pixel density of our sensor array, which is 11.5 dpi, meets the requirements for biometric sensing and soft robotics, typically ranging from 1 to 50 dpi (refer to Table S3, Supporting Information). In addition, ensuring operational robustness under light irradiation is crucial not only for the imager but also for various organic active sensor arrays used in ambient lighting for electronic skin and robotic applications. This study broadens the scope of utilization for organic active sensor matrices.

Flexible large-area imagers hold great promise for pioneering optoelectronic devices customized for a variety of applications. For example, a sheet-type camera can capture images from a wide range of angles simultaneously when deformed, facilitating imaging of surfaces regardless of their geometry.[56] Additionally, curved surface imaging can be applied to a 3D internal scanning mechanism.[57] By utilizing the high-transmission properties of long-wavelength light, such as THz and millimeter waves, this system offers a safer alternative to X-rays for noninvasive internal imaging.[58] Such sheet cameras also find potential applications in eyeball cameras,[59,60] providing several advantages, including a wide range of viewing angles, reduced aberrations, and an extensive focal range. Therefore, our contributions can expand the applications conventionally associated with short-wavelength light to a broader infrared spectrum, introducing functionalities that were previously unattainable.

Infrared light possesses unique capabilities in biochemical analyses, stemming from its high-absorbance characteristics specific to particular substances. For instance, infrared detection can be applied in bioimagers for monitoring temperature, oxygen levels, glucose concentrations, and cellular entities.[61–64] These applications require a broad infrared sensitivity spectrum combined with large-area imaging capabilities, attributes realized by the proposed imager. In previous research, in-liquid glucose and tannic acid were identified through the detection of thermal radiation using a single CNT sensor.[29] Our study has advanced the quantitative detection of glucose solutions, eliminating the need for light sources, sampling, or labeling, while enabling spatial analysis through an imager. This method represents a promising analytical tool with potential applications spanning scientific, industrial, and medical domains. To enhance precision and diversify the range of applications for this biochemical sensing methodology, it is imperative to refine sensitivity, particularly for detecting subtle variations in light intensity.

Enhancing detection efficacy and multifunctionality can be achieved by incorporating specialized technologies tailored for CNT sensors and organic circuits. First and foremost, elevating the sensitivity of CNT sensors is crucial. Techniques such as microfabrication of CNT sensors and thermal design serve as fundamental ways to enhance sensitivity, which can be readily applied to our imager.[41,65,66] Additionally, the integration of antennas[39,67] and metamaterials[68,69] tailored for infrared light can enhance sensitivity by concentrating the electric field. This approach also provides wavelength selectivity, potentially enabling the imager to perform spectroscopic analyses. Organic circuits also hold the potential to enhance the imager's sensitivity. For example, organic differential amplifiers can effectively suppress common-mode noise,[70] facilitating the detection of weak signals without the need for traditional lock-in signal measurement apparatuses. As illustrated in Figure S30, Supporting Information, the differential amplifiers have undergone preliminary testing using the common-source amplifiers presented in this paper, achieving a common-mode reduction ratio of ≈38 dB. Consequently, these amplifiers show promise for increasing the SNR of imagers. The performance characteristics of these organic circuits are significantly influenced by the mobility of the organic semiconductor, emphasizing the importance of high-mobility organic semiconductors in increasing gain and reducing output impedance.[71,72] The integration of these innovative technologies has the potential to advance optical sensing systems across diverse sectors, including medicine and materials science, by enabling the analysis of weak signals independent of measurement apparatuses and ambient conditions.

## 8. Conclusion

A flexible imager was developed through the integration of CNT sensors and organic circuits onto ultrathin Parylene substrates, aiming to enhance infrared imaging sensitivity. When printed on a 2.4-μm-thick Parylene substrate, the CNT sensor exhibited significant enhancement, with a 21-fold increase in output voltage and a 15-fold increase in response speed compared to its counterpart on a thicker glass substrate. This improvement can be attributed to a reduction in thermal capacitance combined with an increase in thermal resistance. Remarkably, the CNT sensors displayed excellent flexibility, consistently retaining their photosensitivity through rigorous bending and crumpling procedures. Shielded OTFTs formed on these Parylene substrates demonstrated exemplary attributes as switching transistors, ensuring stable voltage signal transmission and consistently low off-currents, even under direct light irradiation. When integrated into organic amplifiers and source followers, these OTFTs amplified the THz detection signal tenfold, simultaneously suppressing superimposed hum noise by reducing the output impedance.

Finally, an $8 \times 8$ active matrix comprising CNT sensors and organic circuits was realized, laying the foundation for large-area infrared imaging. This imager not only facilitates quantitative infrared light detection and sequential imaging but also excels in thermal imaging, making it promising for discerning heat sources, tracking biological movement, and analyzing glucose concentrations in liquid media. Our findings indicate that the application spectrum of the proposed imager extends to the infrared domain. The imager holds considerable promise for innovations in biosensing and soft robotics, offering unique infrared capabilities such as advanced thermography and biochemical analysis.

## 9. Experimental Section

*CNT Sensor Fabrication*: CNT sensors were printed on Parylene (diX-SR, Daisan Kasei Co.) substrates, which were formed on a glass-supporting substrate under ambient conditions. A separation layer made of CYTOP (AGC Inc.) was applied to the glass substrate. Parylene substrates of various thicknesses (2.4, 5.4, and 25 µm) were subsequently fabricated through chemical vapor deposition. A solution containing semiconducting and metallic single-walled CNTs (Zeon Co.) was dispenser-printed onto the preheated Parylene substrates at 60 °C. Subsequently, p/n junctions were formed through chemical doping using dispenser printing. The dopant used was prepared by mixing a 0.7 M KOH aqueous solution (Tokyo Chemical Industry Co. Ltd.) with a 0.5 M 15-crown 5-ether aqueous solution (Tokyo Chemical Industry Co. Ltd.). This mixture was printed over half of the previously printed CNT sensors. Connections were established between the CNT sensors, the electrodes, and the OTFTs using flexible Ag paste (ELEPASTE NP1 from Taiyo Ink Mfg. Co., Ltd. and FA-333 from Fujikura Kasei Co., Ltd.). For detailed visualization, the CNT sensors underwent white-light interferometry (VK-X3000, Keyence Corporation) and SEM (SU8240, Hitachi High-Tech Corporation).

*Light Sources*: Seven different light sources were utilized: a frequency multiplier in the THz band ($\lambda = 577$ µm, 100 mW, 4-mm$\varphi$-collimated irradiation, 520- to 532-GHz Custom Modular Tx-Transmitter, Virginia Diodes Inc.), a gas laser in the FIR band ($\lambda = 10.3$ µm, 20-mm$\varphi$-collimated irradiation/1-mm$\varphi$-fiber irradiation, $CO_2$ Laser L4, Access Laser Co.), quantum cascade lasers in the FIR and MIR bands ($\lambda = 6.13$ µm and 4.33 µm, 20 mW, 5-mm$\varphi$-collimated irradiation, DFB-CW QCLs with built-in lenses L12006-1631H-E and L12004-2310H-E, Hamamatsu Photonics K.K.), an LED in the NIR band ($\lambda = 870$ nm, 110 mW, 2-mm$\varphi$-collimated irradiation, L12170, Hamamatsu Photonics K.K.), a laser diode in the NIR band ($\lambda = 1.3$ µm, 130 mW, FPL1053P, Thorlabs, Inc.), an LED emitting white visible light (2.3 mW $cm^{-2}$, GR10-N, Shodensha Co. Ltd.). To enhance the performance of the frequency multiplier, it was equipped with a conical horn antenna, while the other sources had built-in collimation lenses. To maximize the utilization of NIR sources, a 7 × 7 NIR LED matrix was assembled.

*OTFT Fabrication*: For the fabrication of OTFTs, 2.4-µm-thick Parylene films were deposited on a glass substrate that had been pre-coated with a CYTOP layer. A 30-nm-thick Au layer was evaporated onto the Parylene film, serving as the gate electrode. To prepare the surface for the gate dielectric layer, the Au surfaces underwent oxygen plasma treatment. Following this treatment, diX-SR gate dielectrics, ≈50 nm thick, were deposited. Subsequently, a 30-nm-thick DNTT layer was thermally deposited on the gate dielectric. The next step involved the deposition of the source and drain electrodes, which were formed by depositing a 50-nm-thick Au layer onto the semiconductor layer. The OTFTs were then encapsulated with a 500-nm-thick Parylene layer. To ensure optimal shielding, layers of Au (30 nm)/Ag(120 nm)/Au (30 nm) were sequentially deposited. Moreover, a 500-nm-thick Parylene layer was added to insulate this shield layer. The final step involved the deposition of a 50-nm-thick Au layer on the top surface of the OTFTs.

*Transmittance Measurements*: For transmittance measurements, the optical transmittance of the shield layer was assessed using three methods: UV–vis spectroscopy utilizing the SEC2020 spectrometer from ALS Co., Ltd.; FT-IR spectroscopy with the FT/IR 6100FV from Jasco International Co., Ltd.; and THz-TDS with the Pulse IRS 2000-os from Advanced Infrared Spectroscopy Corporation. The measurement wavelength ranges for UV–vis spectroscopy, FT-IR spectroscopy, and THz-TDS were set as 200–1000 nm, 1.4–6.6 µm, and 167 µm–2 mm, respectively. These ranges were chosen to minimize absorption interference from the surrounding air and substrates. For transmittance measurement, the shield layer was deposited on both quartz and sapphire substrates. Each substrate received two layers: Au (30 nm) and Ag (150 nm). Quartz substrate samples were specifically prepared for both UV–vis and THz-TDS measurements, whereas samples on sapphire were solely dedicated for FT-IR analysis.

*Electrical Measurements*: The fundamental characteristics of the OTFTs were assessed using a semiconductor device parameter analyzer (B1500A, Keysight Technologies, Inc.). To study the frequency properties of the organic amplifiers, a fast Fourier transform (FFT) analyzer (CF-9400, Ono Sokki Co., Ltd.) was employed. The input was adjusted to receive 5-$mV_{p\text{-}p}$ sine wave signals ranging from 0.1 Hz to 10 kHz, originating from a power source (B2962A, Keysight Technologies, Inc.). These signals were relayed to the FFT analyzer through the original voltage-follower circuit. Analysis was conducted using 16 384 data points with a Hamming window. For the acquisition of light detection signals from the CNT sensor and the amplified signals, source measurement units (B2912A, Keysight Technologies, Inc.) were utilized. The SNR was calculated as $10\log_{10}({\nu_{signal}}^2/{\nu_{noise}}^2)$, where $\nu_{signal}$ represents the signal voltage, and $\nu_{noise}$ represents the noise voltage. In this context, $\nu_{noise}$ is the cumulative result of the 50-Hz hum-noise power and white-noise power derived from the FFT spectra.

*Imaging Using Active Matrix*: For the 8 × 8 active matrix comprising CNT sensors and OTFTs, signals were acquired through a Bluetooth wireless module. (Figure S18, Supporting Information) This module included A/D converters spanning eight channels and a shift register dedicated to selecting the active matrix's WL. Within the shift register, a voltage of −2.5 V was applied to the selected column, while a voltage of 2.5 V was designated for the non-selected column. The multi-pixel reading speed was calibrated to 1.3 frames per second, deliberately set slower than the maximum speed permitted by the low-pass filter within the A/D converters. The final output images were generated by normalizing the acquired voltage across 256 steps for every pixel.

*Thermal Imaging*: For this procedure, PVC-coated wiring made of tinned copper (EIC-J-S, E-Call Enterprise Co., Ltd.) was used as the heat source. Some of the L-shaped wires were heated through conduction using a soldering iron, while the remaining wires were subjected to Joule heating via resistors rated at 100 Ω and 0.18 A. A thermal camera (FLIR C5, Teledyne FLIR LLC) was employed to accurately record the temperatures of these wires. A BPP film (Origin Ltd.), which allowed light with wavelengths of >5 µm to pass through, was used as the filter.

*Glucose Monitoring*: A glucose mixture was prepared by mixing distilled water and D(+)-Glucose powder (Hayashi Pure Chemical Ind., Ltd.). This solution was then passed through a silicone tube with an internal diameter of 6 mm and an external diameter of 8 mm, driven by a DSP-100SA pump (AS ONE CORPORATION). The flow rate was maintained at 100 dL $min^{-1}$, and the temperature of the solution was maintained at 54 °C using an EWS-100RD hot water bath (AS ONE CORPORATION). To systematically adjust the glucose concentration within the range of 0 to 23 g $dl^{-1}$, 0.15 dl of a concentrated glucose solution (90 g $dl^{-1}$) was sequentially added to 2.5 dl of circulating distilled water. The imaging equipment was positioned beneath the silicone tube, maintaining a 2 mm gap.

## Supporting Information

Supporting Information is available from the Wiley Online Library or from the author.

## Acknowledgements

R. K. and K. L. contributed equally to this work. This study was supported by JSPS KAKENHI (grant nos. JP22H01553, JP21K18721, JP22H00588, JP22K18975, JP22H01940, JP23K19125, JP21H01746, JP21H05809, JP22H01555, JP22H05470, and JP23H00169), JSPS Fellows (grant no. JP22KJ2167), the JST Moonshot R&D Program (grant no. JPMJMS2012), JST FOREST (grant nos. JPMJFR2035 and JPMJFR2022), JST COI-NEXT (grant no. JPMJPF2115), JST ACT-X (grant no. JPMJAX23KL), JST Mirai Program (grant no. JPMJMI23G1), the Inamori Foundation, the Murata Science Foundation, the TEPCO Memorial Foundation, the Strategic Research Development Program of the Kanagawa Institute of Industrial Science and Technology, the Chuo University Personal Research Grant, the Matsuo Foundation, the Sumitomo Electric Groups CSR Foundation, and the Iketani Science and Technology Foundation. The authors gratefully acknowledge Zeon Co., Ltd., Nippon Kayaku Co., Ltd. and Daisan Kasei Co., Ltd. for providing materials and for helpful discussions.

The authors extend their gratitude to the following collaborators for their useful discussions, equipment applications, and assistance during data acquisition: Dr. Koichi Kan, Dr. Masaya Nagai, Mr. Yuto Aoshima, and members of the Advanced Research Infrastructure for Materials and Nanotechnology in Japan (Nanotechnology Open Facilities).

## Conflict of Interest

The authors declare no conflict of interest.

## Data Availability Statement

The data that support the findings of this study are available from the corresponding author upon reasonable request.

## Keywords

carbon nanotubes, flexible electronics, infrared imaging, optical sensors, organic transistors

Received: September 22, 2023
Revised: December 22, 2023
Published online:

[1] K.-J. Baeg, M. Binda, D. Natali, M. Caironi, Y.-Y. Noh, *Adv. Mater.* **2013**, *25*, 4267.
[2] K. Sengupta, T. Nagatsuma, D. M. Mittleman, *Nat. Electron.* **2018**, *1*, 622.
[3] A. Rogalski, *Rep. Prog. Phys.* **2022**, *85*, 126501.
[4] J.-K. Song, M. S. Kim, S. Yoo, J. H. Koo, D.-H. Kim, *Nano Res.* **2021**, *14*, 2919.
[5] H. Zhou, Y. Song, *ACS Appl. Mater. Interfaces* **2021**, *13*, 3493.
[6] D. Yang, D. Ma, *Adv. Opt. Mater.* **2019**, *7*, 1800522.
[7] K. Zhang, Y. H. Jung, S. Mikael, J.-H. Seo, M. Kim, H. Mi, H. Zhou, Z. Xia, W. Zhou, S. Gong, Z. Ma, *Nat. Commun.* **2017**, *8*, 1782.
[8] Y. Wang, Y. Liu, S. Cao, J. Wang, *J. Mater. Chem. C* **2021**, *9*, 5302.
[9] G. Simone, M. J. Dyson, S. C. J. Meskers, R. A. J. Janssen, G. H. Gelinck, *Adv. Funct. Mater.* **2020**, *30*, 1904205.
[10] T. Yokota, T. Nakamura, H. Kato, M. Mochizuki, M. Tada, M. Uchida, S. Lee, M. Koizumi, W. Yukita, A. Takimoto, T. Someya, *Nat. Electron.* **2020**, *3*, 113.
[11] Z. Rao, Y. Lu, Z. Li, K. Sim, Z. Ma, J. Xiao, C. Yu, *Nat. Electron.* **2021**, *4*, 513.
[12] J. Jang, Y.-G. Park, E. Cha, S. Ji, H. Hwang, G. G. Kim, J. Jin, J.-U. Park, *Adv. Mater.* **2021**, *33*, 2101093.
[13] J.-K. Song, J. Kim, J. Yoon, J. H. Koo, H. Jung, K. Kang, S.-H. Sunwoo, S. Yoo, H. Chang, J. Jo, W. Baek, S. Lee, M. Lee, H. J. Kim, M. Shin, Y. J. Yoo, Y. M. Song, T. Hyeon, D.-H. Kim, D. Son, *Nat. Nanotechnol.* **2022**, *17*, 849.
[14] T. Yokota, K. Fukuda, T. Someya, *Adv. Mater.* **2021**, *33*, 2004416.
[15] T. Araki, K. Li, D. Suzuki, T. Abe, R. Kawabata, T. Uemura, S. Izumi, S. Tsuruta, N. Terasaki, Y. Kawano, T. Sekitani, *Adv. Mater.* **2023**, 2304048.
[16] C. Wang, X. Zhang, W. Hu, *Chem. Soc. Rev.* **2020**, *49*, 653.
[17] S. Gielen, C. Kaiser, F. Verstraeten, J. Kublitski, J. Benduhn, D. Spoltore, P. Verstappen, W. Maes, P. Meredith, A. Armin, K. Vandewal, *Adv. Mater.* **2020**, *32*, 2003818.
[18] L. Mei, R. Huang, C. Shen, J. Hu, P. Wang, Z. Xu, Z. Huang, L. Zhu, *Adv. Opt. Mater.* **2022**, *10*, 2102656.
[19] P. Zhu, D. Wu, L. Yin, W. Han, *Opt. Express* **2022**, *30*, 9119.
[20] F. Ellrich, M. Bauer, N. Schreiner, A. Keil, T. Pfeiffer, J. Klier, S. Weber, J. Jonuscheit, F. Friederich, D. Molter, *J. Infrared, Millimeter, Terahertz Waves* **2020**, *41*, 470.
[21] A. S. Kowligy, H. Timmers, A. J. Lind, U. Elu, F. C. Cruz, P. G. Schunemann, J. Biegert, S. A. Diddams, *Sci. Adv.* **2019**, *5*, 36.
[22] S. An, W. Shang, M. Jiang, Y. Luo, B. Fu, C. Song, P. Tao, T. Deng, *Proc. Natl. Acad. Sci. U. S. A.* **2021**, *118*, 2021077118.
[23] P. Bawuah, J. A. Zeitler, *TrAC, Trends Anal. Chem.* **2021**, *139*, 116272.
[24] M. G. Burdanova, A. P. Tsapenko, M. V. Kharlamova, E. I. Kauppinen, B. P. Gorshunov, J. Kono, J. Lloyd-Hughes, *Adv. Opt. Mater.* **2021**, *9*, 2101042.
[25] S. Nandi, A. Misra, *ACS Mater. Lett.* **2023**, *5*, 249.
[26] K. Li, Y. Kinoshita, D. Sakai, Y. Kawano, *Micromachines* **2023**, *14*, 61.
[27] D. Suzuki, S. Oda, Y. Kawano, *Nat. Photonics* **2016**, *10*, 809.
[28] K. Li, R. Yuasa, R. Utaki, M. Sun, Y. Tokumoto, D. Suzuki, Y. Kawano, *Nat. Commun.* **2021**, *12*, 3009.
[29] K. Li, T. Araki, R. Utaki, Y. Tokumoto, M. Sun, S. Yasui, N. Kurihira, Y. Kasai, D. Suzuki, R. Marteijn, J. M. J. Den Toonder, T. Sekitani, Y. Kawano, *Sci. Adv.* **2022**, *8*, eabm4349.
[30] T. Someya, Y. Kato, S. Iba, Y. Noguchi, T. Sekitani, H. Kawaguchi, T. Sakurai, *IEEE Trans. Electron Devices* **2005**, *52*, 2502.
[31] G. H. Gelinck, A. Kumar, D. Moet, J.-L. Van Der Steen, U. Shafique, P. E. Malinowski, K. Myny, B. P. Rand, M. Simon, W. Rütten, A. Douglas, J. Jorritsma, P. Heremans, R. Andriessen, *Org. Electron.* **2013**, *14*, 2602.
[32] B. Bao, D. D. Karnaushenko, O. G. Schmidt, Y. Song, D. Karnaushenko, *Adv. Intell. Syst.* **2022**, *4*, 2100253.
[33] X. Ren, K. Pei, B. Peng, Z. Zhang, Z. Wang, X. Wang, P. K. L. Chan, *Adv. Mater.* **2016**, *28*, 4832.
[34] S. Wang, J. Xu, W. Wang, G.-J. N. Wang, R. Rastak, F. Molina-Lopez, J. W. Chung, S. Niu, V. R. Feig, J. Lopez, T. Lei, S.-K. Kwon, Y. Kim, A. M. Foudeh, A. Ehrlich, A. Gasperini, Y. Yun, B. Murmann, J. B.-H. Tok, Z. Bao, *Nature* **2018**, *555*, 83.
[35] M. Kondo, M. Melzer, D. Karnaushenko, T. Uemura, S. Yoshimoto, M. Akiyama, Y. Noda, T. Araki, O. G. Schmidt, T. Sekitani, *Sci. Adv.* **2020**, *6*, eaay6094.
[36] K. Sim, F. Ershad, Y. Zhang, P. Yang, H. Shim, Z. Rao, Y. Lu, A. Thukral, A. Elgalad, Y. Xi, B. Tian, D. A. Taylor, C. Yu, *Nat. Electron.* **2020**, *3*, 775.
[37] C. Jiang, H. W. Choi, X. Cheng, H. Ma, D. Hasko, A. Nathan, *Science* **2021**, *363*, 719.
[38] R. Kawabata, T. Araki, M. Akiyama, T. Uemura, T. Wu, H. Koga, Y. Okabe, Y. Noda, S. Tsuruta, S. Izumi, M. Nogi, K. Suganuma, T. Sekitani, *Flexible Printed Electron.* **2022**, *7*, 044002.
[39] X. Lu, L. Sun, P. Jiang, X. Bao, *Adv. Mater.* **2019**, *31*, 1902044.
[40] A. Rogalski, *J. Infrared, Millimeter, Terahertz Waves* **2022**, *43*, 709.
[41] D. Suzuki, Y. Takida, Y. Kawano, H. Minamide, N. Terasaki, *Sci. Technol. Adv. Mater.* **2022**, *23*, 424.
[42] D. Suzuki, N. Terasaki, *Sens. Actuators, A* **2023**, *354*, 114296.
[43] W.-Y. Chou, Y.-S. Lin, L.-L. Kuo, S.-J. Liu, H.-L. Cheng, F.-C. Tang, *J. Mater. Chem. C* **2014**, *2*, 626.
[44] S. Lee, M. Mativenga, J. Jang, *IEEE Electron Device Lett.* **2014**, *35*, 930.
[45] A. Axelevitch, B. Gorenstein, G. Golan, *Phys. Procedia* **2012**, *32*, 1.
[46] I. R. Hooper, J. R. Sambles, *Opt. Express* **2008**, *16*, 17258.
[47] M.-J. Spijkman, K. Myny, E. C. P. Smits, P. Heremans, P. W. M. Blom, D. M. De Leeuw, *Adv. Mater.* **2011**, *23*, 3231.
[48] J. Kwon, Y. Takeda, R. Shiwaku, S. Tokito, K. Cho, S. Jung, *Nat. Commun.* **2019**, *10*, 54.
[49] F. Yu, S. Wu, X. Wang, G. Zhang, H. Lu, L. Qiu, *RSC Adv.* **2017**, *7*, 11572.
[50] N. K. Za'aba, D. M. Taylor, *Org. Electron.* **2019**, *65*, 39.
[51] T. Yamamoto, K. Takimiya, *J. Am. Chem. Soc.* **2007**, *129*, 2224.
[52] P.-C. Hsu, A. Y. Song, P. B. Catrysse, C. Liu, Y. Peng, J. Xie, S. Fan, Y. Cui, *Science* **2016**, *353*, 1019.

[53] J. V. Dcosta, D. Ochoa, S. Sanaur, *Adv. Sci.* **2023**, *10*, 2302752.
[54] W. Lee, J. Lee, H. Yun, J. Kim, J. Park, C. Choi, D. C. Kim, H. Seo, H. Lee, J. W. Yu, W. B. Lee, D. H. Kim, *Adv. Mater.* **2017**, *29*, 1702902.
[55] P. Zalar, N. Matsuhisa, T. Suzuki, S. Enomoto, M. Koizumi, T. Yokota, M. Sekino, T. Someya, *Adv. Electron. Mater.* **2018**, *4*, 1870029.
[56] K. Li, D. Suzuki, Y. Kawano, *Adv. Photonics Res.* **2021**, *2*, 2000095.
[57] A. J. J. M. Van Breemen, M. Simon, O. Tousignant, S. Shanmugam, J.-L. Van Der Steen, H. B. Akkerman, A. Kronemeijer, W. Ruetten, R. Raaijmakers, L. Alving, J. Jacobs, P. E. Malinowski, F. De Roose, G. H. Gelinck, *npj Flexible Electron.* **2020**, *4*, 22.
[58] Y. Meng, A. Qing, C. Lin, J. Zang, Y. Zhao, C. Zhang, *Sci. Rep.* **2018**, *8*, 7852.
[59] Y. M. Song, Y. Xie, V. Malyarchuk, J. Xiao, I. Jung, K.-J. Choi, Z. Liu, H. Park, C. Lu, R.-H. Kim, R. Li, K. B. Crozier, Y. Huang, J. A. Rogers, *Nature* **2013**, *497*, 95.
[60] M. Kim, G. J. Lee, C. Choi, M. S. Kim, M. Lee, S. Liu, K. W. Cho, H. M. Kim, H. Cho, M. K. Choi, N. Lu, Y. M. Song, D.-H. Kim, *Nat. Electron.* **2020**, *3*, 546.
[61] C. M. Lochner, Y. Khan, A. Pierre, A. C. Arias, *Nat. Commun.* **2014**, *5*, 5745.
[62] J. Y. Sim, C.-G. Ahn, E.-J. Jeong, B. K. Kim, *Sci. Rep.* **2018**, *8*, 1059.
[63] V. Narayanamurthy, P. Padmapriya, A. Noorasafrin, B. Pooja, K. Hema, A. Y. Firus Khan, K. Nithyakalyani, F. Samsuri, *RSC Adv.* **2018**, *8*, 28095.
[64] T. H. Kim, Z. Zhou, Y. S. Choi, V. Costanza, L. Wang, J. H. Bahng, N. J. Higdon, Y. Yun, H. Kang, S. Kim, C. Daraio, *Sci. Adv.* **2023**, *9*, eade0423.
[65] D. Suzuki, Y. Ochiai, Y. Kawano, *ACS Omega* **2018**, *3*, 3540.
[66] K. Narita, R. Kuribayashi, E. Altintas, H. Someya, K. Tsuda, K. Ohashi, T. Tabuchi, S. Okubo, M. Imazato, S. Komatsubara, *Sens. Actuators, A* **2013**, *195*, 142.
[67] T. Okamoto, N. Fujimura, L. Crespi, T. Kodera, Y. Kawano, *Sci. Rep.* **2019**, *9*, 18574.
[68] B.-X. Wang, C. Xu, G. Duan, W. Xu, F. Pi, *Adv. Funct. Mater.* **2023**, *33*, 2213818.
[69] O. Paul, R. Beigang, M. Rahm, *Opt. Express* **2009**, *17*, 18590.
[70] M. Sugiyama, T. Uemura, M. Kondo, M. Akiyama, N. Namba, S. Yoshimoto, Y. Noda, T. Araki, T. Sekitani, *Nat. Electron.* **2019**, *2*, 351.
[71] K. Liu, B. Ouyang, X. Guo, Y. Guo, Y. Liu, *npj Flexible Electron.* **2022**, *6*, 1.
[72] H. Jiang, W. Hu, *Angew. Chem., Int. Ed.* **2020**, *59*, 1408.